IEEE Access
Multidisciplinary | Rapid Review | Open Access Journal

SPECIAL SECTION ON 5G AND BEYOND MOBILE WIRELESS COMMUNICATIONS ENABLING INTELLIGENT MOBILITY

Received May 27, 2019, accepted July 29, 2019, date of publication August 5, 2019, date of current version August 19, 2019.

Digital Object Identifier 10.1109/ACCESS.2019.2933264

Large-Scale Fading Characteristics and Models for Vehicle-to-Pedestrian Channel at 5-GHz

IBRAHIM RASHDAN[1], (Member, IEEE), FABIAN DE PONTE MÜLLER[1], (Member, IEEE), THOMAS JOST[1], (Member, IEEE), STEPHAN SAND[1], (Senior Member, IEEE), AND GIUSEPPE CAIRE[2], (Fellow, IEEE)

[1]German Aerospace Center (DLR), Institute of Communications and Navigation, 82234 Oberpfaffenhofen, Germany
[2]Department of Electrical Engineering and Computer Science, Technical University of Berlin, 10623 Berlin, Germany

Corresponding author: Ibrahim Rashdan (ibrahim.rashdan@dlr.de)

This work was supported by the DLR basic funding.

ABSTRACT Vehicle-to-Pedestrian (V2P) communication is essential to enable a reliable collision avoidance system for vehicles and vulnerable road users (VRUs). In order to develop a reliable communication system accurate channel models are required. However, no dedicated channel model for V2P communication in critical scenarios has been proposed so far. To develop a channel model, we conducted wideband channel sounding measurements considering a typical collision scenario between a vehicle and a pedestrian in line-of-sight (LoS) and non-LoS (NLoS) situations. The wideband measurement data is used to study the characteristics of large-scale or shadow fading, pathloss and diffraction loss. The spatial correlation of shadow fading is examined and different models are proposed. For NLoS scenario, a 3D scenario model is designed to simulate the diffraction at a row of parked vehicles. The diffraction loss due to parked vehicles is analyzed and modeled based on multiple knife-edge diffraction model combined with a two-ray pathloss model. The results show that the proposed diffraction model provides a good match to the measured pathloss.

INDEX TERMS Channel modeling, pathloss, diffraction, fading, large-scale, shadow fading, spatial correlation, vehicle-to-pedestrian communication.

I. INTRODUCTION

According to the World Health Organization, traffic accidents take about 1.35 million lives and cause more than 50 million injuries each year on the roads of the world. In 2018, vulnerable road users (VRUs), including pedestrians, cyclists and motorcyclists, accounted for almost half of the road victims [1]. It has been found through experiments and simulations that intelligent transportation system (ITS) applications have been successful in increasing road safety [2], [3]. However, VRUs received less attention than vehicles. Most recent studies which address VRU protection focus on driver assistance systems that only rely on on-board perception sensors to detect and locate other surrounding traffic participants [4]–[6]. However, radar sensors, laser-scanners and camera-based systems have critical limitations due to the need for line-of-sight (LoS) and the weather-related performance. To enhance safety and mobility of VRUs, vehicle-to-pedestrian (V2P) communication enables a collision avoidance system by establishing direct communication between vehicles and VRUs. Using V2P communication can improve mutual detection, localization and tracking of both vehicles and VRUs and generate appropriate warnings to prevent accidents.

In order to develop a reliable V2P communication system, accurate channel models are of immense importance. Vehicle-to-vehicle (V2V) and vehicle-to-infrastructure (V2I) channels were extensively studied in the last years, and various channel models were proposed. However, to the best of our knowledge, a dedicated V2P channel model in critical scenarios does not exist yet. To derive accurate models, V2P channels have to be thoroughly investigated. These channel models should be able to reproduce reliably and with low complexity the time-variant behavior of the channel characteristics. Since the vehicle is a common element in V2V, V2I and V2P, some similarities could arise in the propagation channel. However, also important differences are identified. Assuming that a safety system based on V2P communication is incorporated in the pedestrian's smartphone, the following characteristics will have a direct impact on the V2P propagation channel:

1) The mobility pattern of the pedestrian.
2) The changing antenna height and orientation depending on the smartphone's location and pedestrian's activity (texting, phoning, etc).

The associate editor coordinating the review of this manuscript and approving it for publication was Cesar Briso.

3) The relatively low height of the pedestrian's smartphone antenna, such that the LoS could be partially or completely obstructed by road side objects, e.g. trees, moving or parked vehicles and surrounding pedestrians.

All these aspects need to be accounted for when developing the channel model. Therefore, we conducted a wideband V2P channel measurement campaign considering a collision scenario between a vehicle and a pedestrian. The goal of this work is to bring detailed characterizations of shadow fading for the V2P channel in LoS and non-LoS (NLoS) scenarios. The main contributions of this paper can be summarized as follows:

1) Pathloss models for LoS and NLoS scenarios are proposed.
2) To model the diffraction loss and gain deep insight into the propagation under NLoS conditions, we developed a 3D tool to detect the diffraction edges and calculate the diffraction loss.
3) The spatial correlation of shadow fading is investigated and modeled.

The paper is organized as follows: After a review of prior work in Section II, we describe the channel measurement setup and scenarios in Section III. Section IV presents the model of the pathloss, the diffraction loss as well as the spatial correlation of shadow fading. Finally, conclusions are drawn in Section V.

II. RELATED WORK

Few recent studies tackled the subject of V2P communications recently. Rashdan *et al.* in [7] presented pathloss models for LoS and NLoS scenarios based on a V2P wideband channel measurement campaign. The authors found that the two-ray pathloss model fits the measured pathloss for the LoS scenario in case of a static receiver (Rx). In case of a moving pedestrian, the authors reported that the multipath components (MPCs) from the pedestrian body caused rapid fluctuations of the pathloss. The extra attenuation due to surrounding pedestrians as well as due to parked vehicles was also studied, but the diffraction loss was not modeled. Also Makhoul *et al.* performed V2P channel measurement in [8]. Based on the measurement in LoS scenario, the authors presented a two-ray pathloss model for the strongest path contribution and log-distance pathloss model for the pathloss of discrete scatterers. Normal and Ricean distributions for large and small scale fading respectively were also reported. In [9], the authors investigated the first-order characteristics of the V2P channel at 5.8 GHz in a business district environment. The K-factor was calculated for different locations of the transmitter (Tx) and Rx antennas and vehicle speeds. However, their work was based on narrowband RSSI measurements.

Further work related to V2P communication can be found in the literature. However, they only focus on evaluating the performance of V2P communication systems based on narrowband measurements and simulations. For instance the authors in [10] conducted a study on the applicability of WiFi-based communication for V2P scenarios. The authors evaluated the performance of the communication in terms of packet delivery ratio (PDR) and packet inter-reception time. Based on experiments, they found out that, in order to satisfy a collision avoidance application, a transmission rate greater than 1 Hz is required. In [11], the performance of IEEE 802.11p-based V2P communication was evaluated and compared with WiFi and cellular-based communication. The PDR and end-to-end latency in LoS and NLoS scenarios were calculated. The authors reported that LTE-based communication has better PDR than IEEE 802.11p while the latter showed a lower latency. WiFi-based communication showed worse performance than the IEEE 802.11p in terms of both, PDR and latency. Honda and Qualcomm developed an IEEE 802.11-based pedestrian safety system in [12]. They implemented a DSRC stack within the WiFi chipset on a smartphone. To lower the smartphone's power consumption, a false-alarm suppression algorithm was developed. The communication performance was studied in terms of RSSI and inter-reception time. Jutila *et al.* addressed the use of IEEE 802.11p-based communication between VRUs and vehicles [13]. The authors conducted experiments using Cohda MK4 communication units. They found out that the obstacles located between the Tx and the Rx had a severe impact on the achievable communication range. The authors in [14] considered an intersection scenario at which they evaluated the performance of the IEEE 802.11p-based V2P communication for crash avoidance application through simulations. Their results showed that even in scenarios with relatively low channel load, there was a significant loss of packets. The authors in [2] verify the significant packet loss in their simulations and showed that a lower packet inter-reception time is achieved by choosing higher-order modulations in IEEE 802.11p. Several publications presented system concepts for VRUs protection such as [15]. A number of other studies proposed using cellular-based communication to enable VRU protection (e.g., [16] and [17]).

III. CHANNEL MEASUREMENTS

In this section we describe the V2P measurement campaign which is the basis to develop the V2P channel model. Further details on the measurement campaign itself can be found in [7].

A. MEASUREMENT SETUP

The measurement campaign was carried out in March 2017 on the runway of the airport in Oberpfaffenhofen near Munich, Germany. The runway represents a controlled environment due to the absence of nearby objects/buildings that might cause reflections. LoS and NLoS propagation scenarios were considered. Since our motivation is to develop a V2P channel model to support the development of collision avoidance systems, a collision scenario of a vehicle and a pedestrian was emulated. Fig. 1 shows the measurement environment and the trajectory of both, the test vehicle and the pedestrian. According to the figure, both the vehicle and the

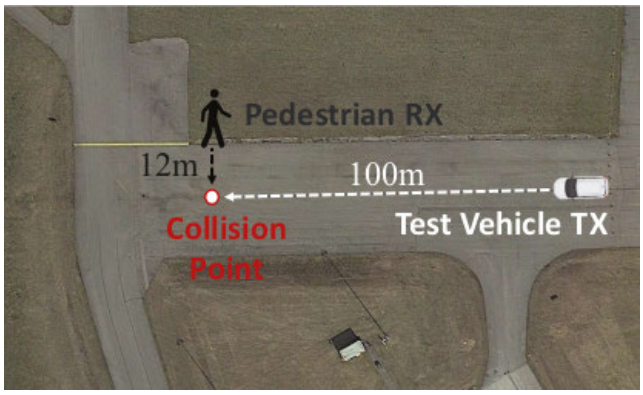

FIGURE 1. Aerial view of the measurement scenario showing the trajectories of the Tx and the Rx towards the imaginary collision point. (Google Maps 2017 Geobasis-de/BKG.)

pedestrian trajectory intersect at an imaginary collision point. In all experiments, the test vehicle (Mercedes G400) (Fig. 2a) transmits signals which are received by an antenna held by a pedestrian or mounted on a tripod (Fig. 2b). In this paper, only the scenarios with a static tripod will be considered for analysis.

(a) Tx Test Vehicle (b) Rx Tripod

FIGURE 2. Tx and Rx involved in the measurement campaign.

The V2P measurement campaign was carried out using the RUSK-DLR channel sounder with parameters summarized in Table 1. The channel sounder transmitted measurement signals at a carrier frequency of 5.2 GHz, which is close to the 5.9 GHz ITS band. The bandwidth was 120 MHz which results in a delay resolution of 8.33 ns. The channel transfer function was recorded every 1.024 ms, allowing to resolve a maximum Doppler shift of 488 Hz.

TABLE 1. Channel sounder parameters.

Parameter	Value
RF center frequency	5.2 GHz
Bandwidth B	120 MHz
Transmit power	37 dBm
Signal period T_p	0.8 µs
Time grid T_g	1.024 ms
Tx antenna	Onmi-directional (V-polarized), 8 dBi
Rx antenna	Omni-directional (V-polarized), 8 dBi
Vehicle speed	≈11 m/s
Pedestrian speed	≈1.2 m/s

GNSS receivers were used to record the position of both the Tx and Rx antennas as a ground truth. The vehicle, the tripod and the pedestrian were equipped with a Topcon Legacy E+ L1/L2 GLONASS/GPS receiver. A geodetic-grade GNSS antenna was placed on the roof of the vehicle, on one end of the tripod and attached to the helmet of the pedestrian (see Fig. 2). The 10 Hz recorded GPS and GLONASS raw data was post processed to provide carrier-fixed solutions with centimeter-level accuracy. To determine the location of the parked vehicles during the obstructed LoS test, an LDMRS multi-layer laser scanner from Sick was attached to the front bumper of the test vehicle combined with a Ublox LEA 4T GPS receiver. In post-processing, the resulting point cloud was transformed from a vehicle coordinate frame to a global coordinate frame using the code-fixed solution of the Ublox LEA 4T GPS receiver.

To time synchronize the GNSS positions with the high rate channel sounder measurement data cubic spline interpolation has been used on the positioning data. The displacement between GNSS and the Tx antenna of the sounder, as shown in Fig. 3, was taken into account when computing the position of the Tx antenna, i.e. a correction is performed to shift the GNSS position by distance d_Δ and angle θ. In a similar way, the calculation of the Rx antenna position based on the GNSS position is performed.

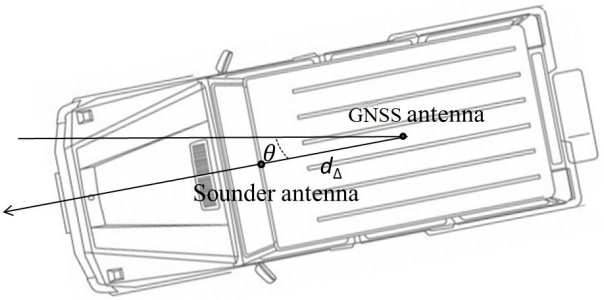

FIGURE 3. Top view of the vehicle carrying the transmitter showing the location of the channel sounder and the geodetic-grade GNSS antenna.

B. MEASUREMENT SCENARIOS

The test vehicle moved around 100 m with an average speed of 11 ms^{-1} towards the collision point. The pedestrian equipped with the receive antenna walked around 12 m towards the collision point with an average speed of 1.2 ms^{-1}. To study a realistic V2P signal propagation, we measured the channel in different LoS and NLoS scenarios, with both a static tripod and a moving pedestrian. In this work, we focus on the two following scenarios:

- In Fig. 4a the experiments with a static tripod are used as a reference for ideal LoS propagation conditions.
- In Fig. 4b the NLoS scenario is shown, where six vehicles of different sizes and shapes are placed parallel to the trajectory of the test vehicle to study the impact of parked vehicles on the signal propagation and especially the LoS blockage. The vehicles are parked 1 m apart

(a) LoS with tripod (b) NLoS with static tripod

FIGURE 4. **Measurement scenarios addressed in this paper.**

from each other. The Rx antenna is placed on a tripod at a height of 1.1 m and a distance from the collision point of 7 m. The reason for choosing the scenario with a static tripod and not a moving pedestrian is to exclude the effect of movement and to study only the propagation loss due to the obstruction of the LoS.

IV. CHANNEL MODEL

In this section, we present pathloss models for the LoS and the NLoS scenarios. The diffraction loss due to blockage of the LoS from the parked vehicles in the NLoS scenarios is investigated and modeled. A 3D tool is developed to calculate the diffraction loss and verify the proposed model. Finally, shadow fading is extracted from the measurement data and its spatial correlation is modeled in the LoS and the NLoS scenarios.

The channel impulse response (CIR) can be expressed mathematically as a sum of $N(t)$ Dirac impulses [18]:

$$h(t,\tau) = \sum_{i=0}^{N(t)-1} \alpha_i(t) \cdot \delta_i(\tau - \tau_i(t)), \tag{1}$$

where $\alpha_i(t)$ and $\tau_i(t)$ are the complex amplitude and the delay of the i-th MPC at time step t and $\delta(\cdot)$ is the Dirac function. The instantaneous power delay profile (PDP) is then calculated by:

$$P(t,\tau) = |h(t,\tau)|^2, \tag{2}$$

where $|h(t,\tau)| = \sqrt{(I_h(t,\tau))^2 + (Q_h(t,\tau))^2}$, where $I_h(t,\tau)$ and $Q_h(t,\tau)$ are the real part and the imaginary part of the complex amplitude $\alpha_i(t)$ [19]. Next, the average PDP (APDP) $\overline{P(t,\tau)}$ is obtained by applying a sliding window on the PDP with a length of $l_w = 10\lambda$,* which is equivalent to $N_{\text{av}} = \frac{l_w}{v \cdot T_g} = 51$ PDPs, where $v = 11$ ms^{-1} is the average velocity of the transmitter, $T_g = 1.024$ ms is the time grid, and λ is the wavelength. Within each segment of 10λ, the channel is assumed to be quasi-stationary.

Based on the APDP, the received power $P_r(t)$ can be calculated as:

$$P_r(t) = \sum_{i=0}^{N(t)-1} \overline{P(t,\tau_i)}. \tag{3}$$

*Different window sizes are tested, a window size of 10λ is found to best fit our data. It provides a sufficient number of samples to accurately extract the small-scale fading [20].

Thereafter, the path loss P_L is obtained by:

$$P_L = \frac{P_t G_{Tx} G_{Rx}}{P_r}, \tag{4}$$

where P_t, P_r, G_{Tx}, and G_{Rx} are the transmitted power, received power, Tx antenna gain and Rx antenna gain, respectively. The path loss consists of two components, namely, the distance-dependent pathloss model and shadow fading. This is expressed in logarithmic scale as:

$$P_L[\text{dB}] = \underbrace{P_{L0} + 10n\log_{10}(d/d_0)}_{\text{log-distance pathloss model}} + \underbrace{\chi[\text{dB}]}_{\text{shadow fading}}, \tag{5}$$

where P_{L0} is the pathloss at the reference distance d_0 and n is the pathloss exponent. The first component is the signal attenuation due to the separation between Tx and Rx. Shadow fading is caused by shadowing processes and leads to a change in the local mean of the path loss over relatively large distances. Whereas the small-scale fading is the variation due to the superposition of multiple propagation paths. It leads to power variations when moving over relatively short distances in the order of the signal wavelength. The small-scale fading is extracted by applying the aforementioned sliding window.

A. PATHLOSS MODEL

The two-ray ground reflection pathloss model has been reported to fit well to the measured pathloss in LoS scenarios [7], [8], and [21]. Fig. 5 shows the measured pathloss versus the Tx-Rx distance. Both the log-distance pathloss model and the two-ray pathloss model are visualized. It can be seen that the two-ray pathloss model provides a good fit to the measured pathloss even at short distances with a shadow fading standard deviation of $\sigma = 0.68$dB. We estimated the relative permittivity for the ground as $\epsilon_r = 1.05$ which is close to the values reported in [22]. Details about the model can be found in [7]. The parameters of the log-distance pathloss model are estimated in a minimum mean square error sense and listed in Table 2.

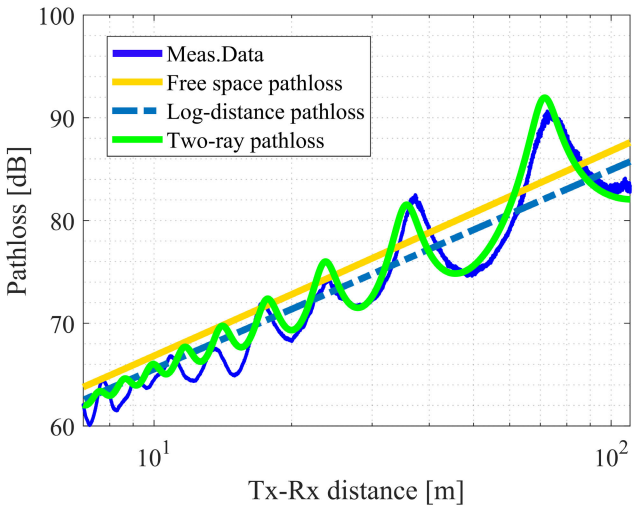

FIGURE 5. **Measured and modeled pathloss for LoS scenario.**

TABLE 2. Log-distance pathloss model parameters based on wideband measurement data.

Scenario		d_0 [m]	n	$P_L(d_0)$ [dB]	σ [dB]
LoS		1	1.94	46.77	3.19
NLoS	**OLoS part**	1	1	73	4.35
	LoS part	1	2	46.77	4.35

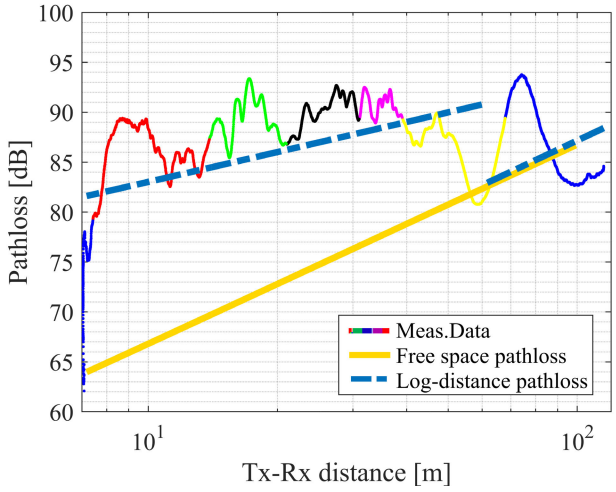

FIGURE 6. Measured and modeled pathloss for NLoS scenario.

Fig. 6 shows the measured pathloss and the proposed pathloss model for the NLoS scenario. The pathloss samples displayed by the colored curve correspond to the pathloss during the LoS (blue) or to an obstructed LoS by a specific parked vehicle (yellow, magenta, black, green and red). It can be noticed that compared to the free space pathloss (FSPL) model, the obstruction of the LoS causes an extra loss between 10 - 20 dB depending of the size of the parked vehicle. Between Tx-Rx distances of 7 m to 60 m the pathloss experiences large values due to obstruction by the parked vehicles. Therefore, we divided the pathloss model into LoS and OLoS parts. Each part has a different pathloss exponent n and standard deviation σ.

Table 2 summarizes the results of fitting the measured data linearly to the log-distance pathloss model for LoS and NLoS scenarios. Note that the FSPL model has $n = 2$ and $P_L(d_0) = 46.77$dB and is plotted for comparision in Fig. 6. The parameters of the log-distance pathloss model for both the LoS scenario and the LoS part of the NLoS scenario are similar to those of the FSPL model. On the other hand, the pathloss exponent $n = 1$ during the obstruction of the LoS indicates that the power decreases slower than during LoS situation, however, with more shadowing caused by the parked vehicles, i.e., a higher value of $P_L(d_0) = 73$dB. A similar inverse proportional relation between n and $P_L(d_0)$ is reported in [7].

B. DIFFRACTION

When the LoS path between the Tx and the Rx is obstructed in the Fresnel zone by an obstacle whose dimensions are larger than the wavelength of the radio wave, the measured propagation pathloss is increased. The additional increase in attenuation is due to the blockage of the LoS by the obstacles and the signal is received by diffraction of the electromagnetic waves. According to Huygens principle, the electric field is the sum of the Huygens sources located in the plane above the obstruction [23]. The calculation of the diffraction loss can be done by treating the obstacles as absorbing knife-edges [23]. Applying this simplification, the diffraction loss (in dB) becomes a function of only the Fresnel-Kirchoff parameter v as:

$$L_i = -20\log\left(\frac{\sqrt{[1-C(v)-S(v)]^2+[C(v)-S(v),]^2}}{2}\right) \tag{6}$$

where $C(v)$ and $S(v)$ are the Fresnel cosine and sine integrals.

The complex Fresnel integral is given by:

$$F(v) = \int_0^v \exp\left(j\frac{\pi t^2}{2}\right) \mathrm{d}t = C(v) + jS(v), \tag{7}$$

The Fresnel cosine and sine integrals are given by:

$$C(v) = \int_0^v \cos\left(\frac{\pi t^2}{2}\right) \mathrm{d}t \tag{8}$$

$$S(v) = \int_0^v \sin\left(\frac{\pi t^2}{2}\right) \mathrm{d}t \tag{9}$$

The sine and cosine integrals can be calculated by using their Taylor expansions as in [24],

$$C(v) = \sum_{m=0}^{\infty} c_m v^{4m+1}, \quad c_0 = 1,$$
$$c_{m+1} = \frac{-\pi^2(4m+1)c_m}{4(2m+1)(2m+2)(4m+5)} \tag{10}$$
$$S(v) = \sum_{m=0}^{\infty} s_m v^{4m+3}, \quad s_0 = \frac{\pi}{6},$$
$$s_{m+1} = \frac{-\pi^2(4m+3)s_m}{4(2m+2)(2m+3)(4m+7)} \tag{11}$$

The Fresnel-Kirchoff parameter v depends on the distance d_1 from the Tx to the diffracting edge, the distance d_2 from the diffracting edge to the Rx and the effective height h of the diffracting edge:

$$v = h\sqrt{\frac{2(d_1+d_2)}{\lambda d_1 d_2}}. \tag{12}$$

To calculate the diffraction loss over multiple knife edges, the Epstein-Peterson method is used [25], which is illustrated in Fig. 7. This method is found to give the best results for the given geometry. In this method, the total diffraction loss is the sum of the k losses on all edges:

$$L_{tot} = \sum_{i=1}^{k} L_i. \tag{13}$$

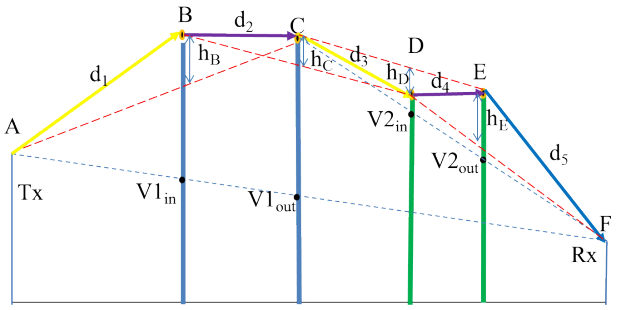

FIGURE 7. The Epstein-Peterson method for four edges. For the edge B, the geometrical parameters (d_1, d_2, h) in (12) are (d_1, d_2, h_B). Similarly, for edge C, the geometrical parameters (d_1, d_2, h) in (12) are (d_2, d_3, h_C). This figure can be seen as a 2D projection of the 3D model in Fig. 9.

When calculating the loss due to diffraction from the first edge, the second edge is considered as a receiver and then to calculate the loss on the second edge, the first edge is considered as a transmitter and the third edge as a receiver and so forth.

Hence, modeling the diffraction loss requires computing the geometrical parameters d_1, d_2 and h for the diffraction process at each edge. This can be done by accurately modeling the size of the objects and their distribution in the propagation environment. To this end, we have developed a 3D tool as illustrated in Fig. 8, which comprises the following steps:

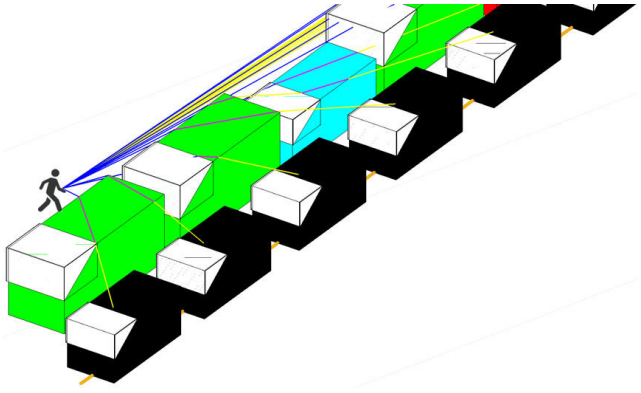

FIGURE 8. Snapshot from the 3D modeling tool.

(a) Modeling static objects in the environment is done by importing the objects dimensions and locations from the laser scanner measurements and the positions of Tx and Rx from the GNSS measurements. The vehicles are represented by a cuboid and the vehicle front-end is represented by a triangular prism.

(b) A direct ray from the Tx to the Rx is created, then intersections between this ray and the objects in the environment are detected as illustrated in Fig. 9.

(c) If the ray intersects with an object, two intersection points will result, entering point and exiting point. The diffraction points are found by projecting the intersection points on the roof of the object. For simplicity, only roof diffraction is considered.

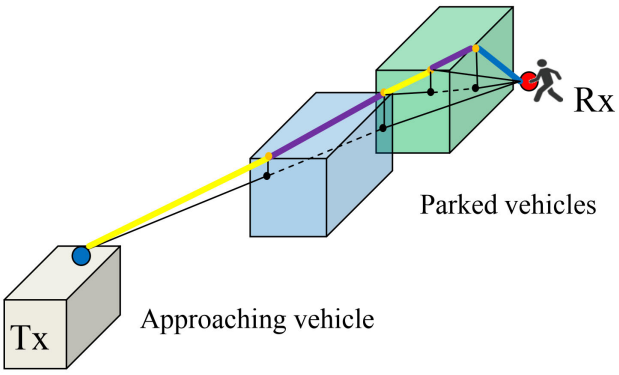

FIGURE 9. 3D illustration of the modeling procedure.

(d) The exiting point is then treated as a secondary transmitter and the previous step is repeated to check further intersections with other objects and find the other diffraction points.

(f) The diffraction loss is then calculated at each diffraction point and summed up to get the total diffraction loss.

(g) The diffraction loss is combined with two-ray pathloss model or a FSPL to get the total propagation loss.

In Fig. 10 we compare the measured pathloss within the obstruction region to the modeled pathloss using the combined two-ray pathloss model and the multiple knife-edge diffraction model. Despite its simplicity, the proposed model is able to provide a match for the pathloss with a standard deviation $\sigma = 4$ dB when considering a line of parked vehicles between a vehicle and a pedestrian. The discontinuity of the model's curve occurs when the the number of parked vehicles blocking the LoS is changed due to the movement which will result in an increase or decrease in the number of diffraction edge.

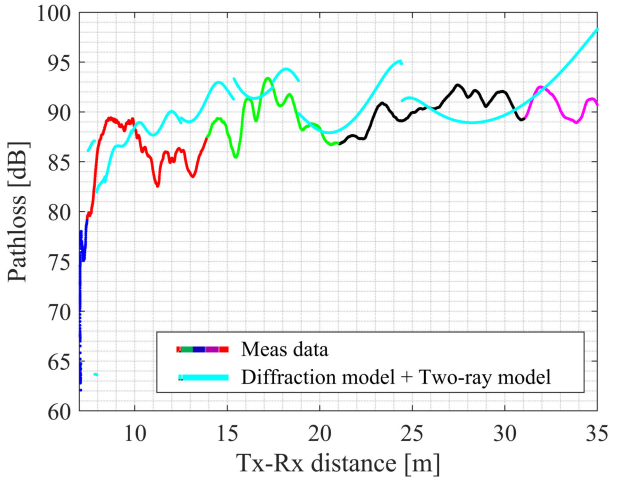

FIGURE 10. The measured pathloss during obstruction of the LoS, and the modeled pathloss as a summation of the multiple knife-edge diffraction model and the two-ray pathloss model.

C. SPATIAL CORRELATION OF SHADOW FADING

Shadow fading is extracted by removing the impact of the small-scale fading and subtracting the path loss model from the measured PDPs by averaging using a sliding window of length $l_w = 10\lambda$. This window size is found to provide a sufficient number of samples to accurately extract the small-scale fading and calculate the decorrelation distance of shadow fading. Fig. 11 shows the extraction of shadow fading from the measured pathloss for the NLoS scenario using a window size of 10λ.

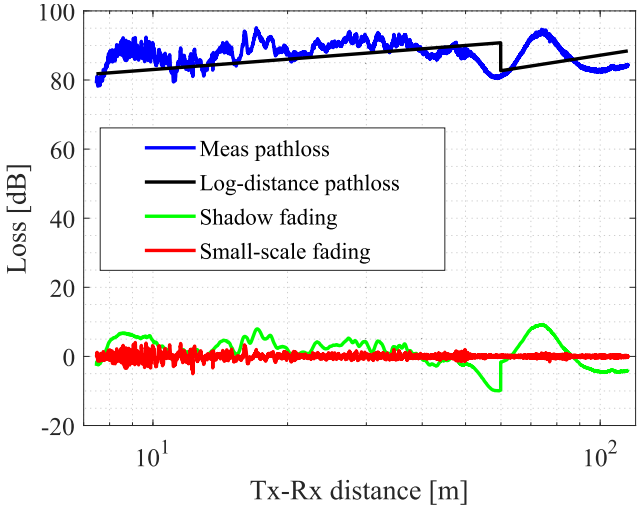

FIGURE 11. An exampale of the extraction of shadow fading from the measured pathloss for the NLoS scenario using a window size of 10 λ.

Shadow fading is strongly dependent on the environment, i.e. it varies from one area to another. Movements of the vehicle, the pedestrian and the surrounding scatterers result in a dynamic environment. When the receiver moves to a shadowed area, it remains shadowed for some time or corresponding traveled distance. This implies that shadowing is spatially correlated. Due to this underlying correlation, consecutive packet losses can occur during this interval. As a result, communication performance will be affected. Therefore, accurate modeling of the spatial correlation of shadow fading is important to design reliable V2P communication system. Models are used to generate realizations of shadow fading process with the desired correlation in simulations. Different techniques for generating shadow fading based on the correlation models can be found in literature, such as [26], [27]. In what follows, we investigate the spatial correlation of shadow fading for the LoS and the NLoS scenarios. The NLoS scenario is further divided into LoS part (parked vehicles are not obstructing the LoS) and OLoS part (six parked vehicles are obstructing the LoS). The LoS part covers the Tx-Rx distance which is larger than 60 m, while the OLoS part covers the Tx-Rx distance equal to or less than 60 m. The spatial correlation can be obtained by the autocorrelation of shadow fading as:

$$r(\Delta d) = \mathrm{E}\left[\chi(d)\chi(d+\Delta d)\right], \tag{14}$$

where d is the distance between Tx and Rx, and Δd is the distance between two observed positions. $\mathrm{E}[\cdot]$ denotes the expected value of $[\cdot]$. The estimation of the autocorrelation function of any random process requires having a large set of samples at every observation time t to calculate the statistical average or the so called ensemble average. By assuming ergodicity of a random process i.e., the sample average over time t for one realization (measurement runs) of the random process converges to the ensemble average as the length of the realizations tends to infinity, the autocorrelation function can be calculated by using samples collected from one measurement run.

1) STATIONARITY TEST

A random process is called wide sense stationary (WSS) when the mean and the autocorrelation do not vary with time. Shadow fading can be assumed stationary since the distance-dependent part is subtracted from the measured pathloss when extracting shadow fading [28]. However, to prove the stationarity assumption, we put the shadow fading under test, namely, the modified reverse arrangement test (MRA) [29]. The MRA test is performed by dividing the shadow fading sample record into N_s equal segments and calculate the square mean value in each segment $(x_1^2, x_2^2, x_3^2, \ldots x_{Ns}^2)$. In a stationary random process the square mean values of adjacent segments are independent [29] and any time trend will result in non-stationarity. The test checks if the examined random process has a time trend by calculating how many times, starting with x_1^2, that each subsequent square mean value $(x_2^2, x_3^2, \ldots x_{Ns}^2)$ is less than x_1^2. This step is repeated with each square mean value. Each inequality is called a 'reverse arrangement'. Fig. 12 shows an example of the mean square values of shadow fading (SF) for $N_s = 10$ segments and $N_s = 20$ segments which correspond to distance interval of 5 m and 10 m for both the LoS and the NLoS scenarios. It can be seen that the changes in the mean value do not follow a specific trend. The total number of the reverse arrangements A is then used to calculate the total score as

$$z = \frac{A - \left[\frac{N_s(N_s-1)}{4}\right]}{\sqrt{\frac{2N_s^3+3N_s^2-5N_s}{72}}}. \tag{15}$$

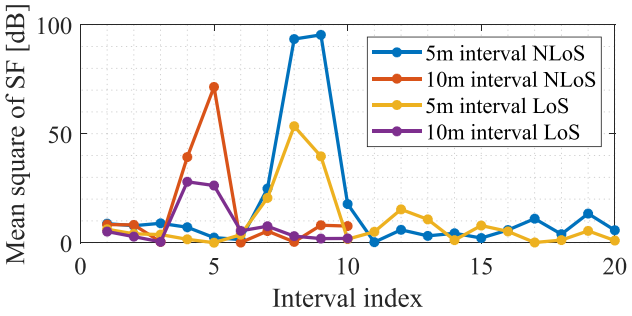

FIGURE 12. Mean square value of shadow fading calculated within intervals of 5 m and 10 m for the LoS and NLoS scenarios.

The stationarity hypothesis is then verified with 5% significance if the absolute value of the total score $-1.96 \leq z \leq 1.96$. Fig. 13 shows the z score of the MRA test for 60 different number of intervals N_s. It can be seen from that both LoS and NLoS scenarios as well as the two parts of the NLoS scenario pass the stationarity test.

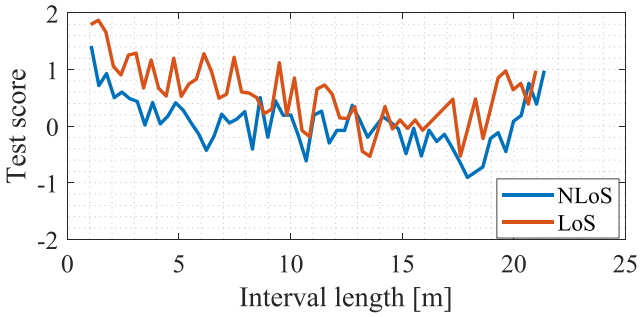

(a) LoS and NLoS scenarios

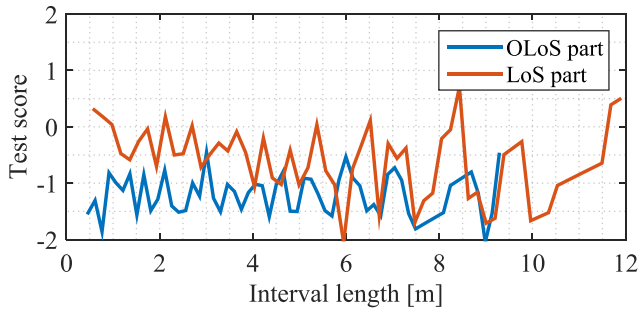

(b) LoS and OLoS parts of the NLoS scenario.

FIGURE 13. Score of the MRA stationarity test.

We estimated the autocorrelation functions from the measurement data using (14). Fig. 14 shows the estimated autocorrelation functions with respect to Δd.

The decorrelation distance d_c is defined as the value of Δd at which the value of the normalized autocorrelation function drops to e^{-1}. The decorrelation distance is scenario-dependent and indicates how fast shadow fading is changing over distance. Shadow fading can be assumed to stay constant within the decorrelation distance d_c. Applying this assumption, shadow fading can be considered as a block fading which leads to a simplification of shadow fading modeling in simulators.

Fig. 14a illustrates the spatial autocorrelation function of shadow fading for the LoS and NLoS scenarios. It can be seen that the decorrelation distance in the LoS scenario is 7.2 m. Blocking the LoS by parked vehicles leads to larger decorrelation distance of 10.4 m. This implies that compared to the LoS, shadow fading in the NLoS experiences less variation i.e., similar diffraction loss, when the LoS is obstructed by the same object. The oscillation pattern in both scenarios can be explained by the constructive and destructive interference which are due to the superposition of the direct and the ground-reflected rays, (see Fig. 5 and Fig. 6).

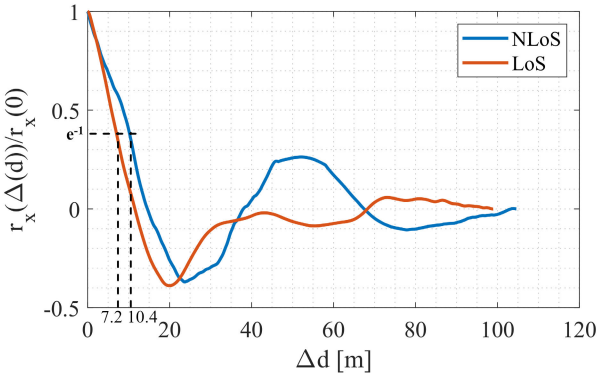

(a) Normalized autocorrelation function for shadow fading for the LoS and the NLoS scenarios

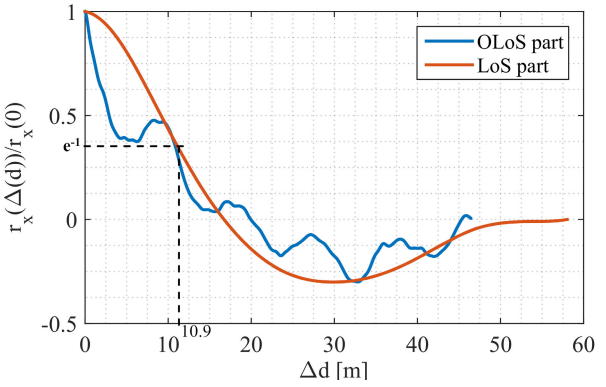

(b) Normalized autocorrelation function for shadow fading for the LoS part and the OLoS part of the NLoS scenario.

FIGURE 14. Normalized empirical spatial autocorrelation function of shadow fading for the LoS, NLoS scenarios and the two parts of the NLoS scenario.

The spatial autocorrelation function of shadow fading for both LoS and OLoS parts of the NLoS scenario are illustrated in Fig. 14b. Both the LoS and the OLoS parts have nearly similar decorrelation distances of 10.7 m and 10.9 m, respectively. However, shadow fading in the OLoS part experiences less correlation than the LoS part when $\Delta_d < 10$ m. This indicates that shadow fading varies faster compared to the LoS part within $\Delta_d < 10$ m, as can be seen in Fig. 11.

We fitted the empirical autocorrelation function to three theoretical autocorrelation function models, the first model is the classical model proposed by Gudmundson [30] which is based on a single negative exponential function,

$$r(\Delta d) = \exp\left(-\frac{|\Delta d|}{d_{c1}}\right), \tag{16}$$

where d_{c1} is the decorrelation distance. The second model is the double exponential model which is also a well-known and widely used model [31]. It models the spatial correlation as a sum of two negative independent exponential functions,

$$r(\Delta d) = \alpha \exp\left(-\frac{\Delta d}{d_{c2}}\right) + (1-\alpha)\exp\left(-\frac{\Delta d}{d_{c3}}\right), \tag{17}$$

where $d_{c2} > 0$, $d_{c3} > 0$ and the weight factor $0 \leq \alpha \leq 1$ are tunable parameters. The third model is the exponential

decaying sinusoid model [32] and is given by

$$r(\Delta d) = \exp\left(-\frac{\Delta d}{d_{c4}}\right)\left[\cos\left(-\frac{\Delta d}{d_{c5}}\right) + \frac{d_{c5}}{d_{c4}}\sin\left(-\frac{\Delta d}{d_{c5}}\right)\right], \tag{18}$$

where $d_{c4} > 0$ and $d_{c5} > 0$ are tunable parameters. The tunable parameters in (17) and (18) are estimated in a MMSE sense.

From Fig. 15 and Fig. 16 and Table 3, it can be found that the single and the double exponential model can loosely follow the trend of the empirical autocorrelation function. The double exponential model performs slightly better than the exponential model with two parameters to be estimated rather than one. The exponential decaying sinusoid model provides better match to the empirical autocorrelation function in all scenarios except for the OLoS part in Fig. 16b where all three models provide a fit with a nearly similar standard deviation σ.

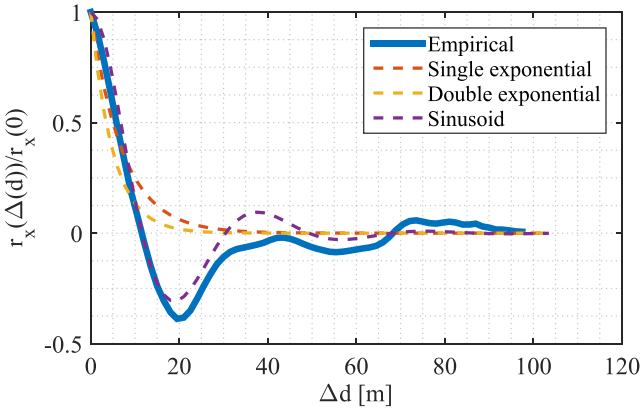

(a) LoS scenario.

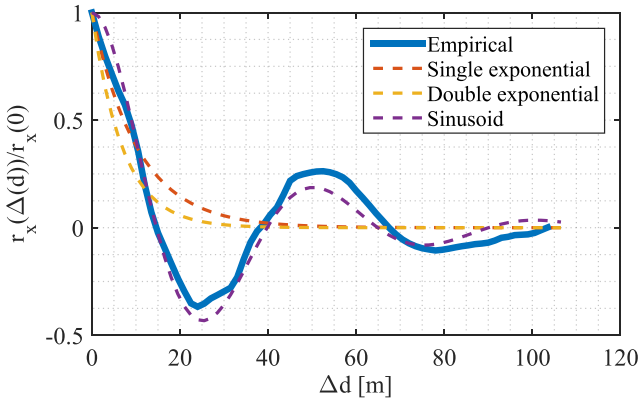

(b) NLoS scenario.

FIGURE 15. Normalized empirical spatial autocorrelation function of shadow fading for the LoS and NLoS scenarios, and the corresponding fitting models.

D. MODEL IMPLEMENTATION

The pathloss models included in this work can be applied in simulations for the given scenarios to predict the pathloss and the received power at each Tx and Rx position. The additional loss due to the obstruction of the LoS can be calculated by implementing the method of detecting the diffraction edges provided in this paper and then calculating the knife-edge diffraction loss. This provides a more accurate prediction of the received power in the presence of an obstruction from a parked vehicle. Additionally, for more realistic simulation, the spatial correlation of shadow fading need to be considered when generating shadow fading map. To generate

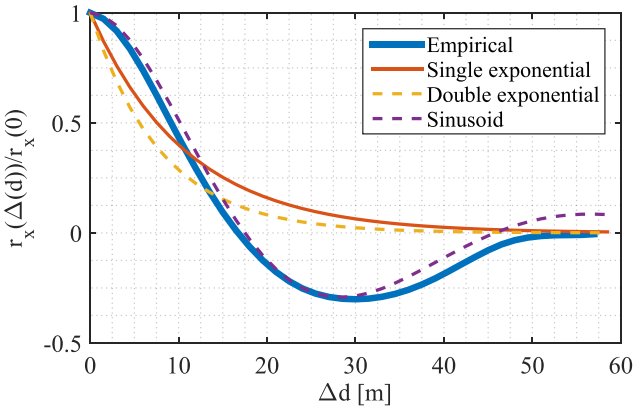

(a) LoS part (No vehicles are obstructing the LoS).

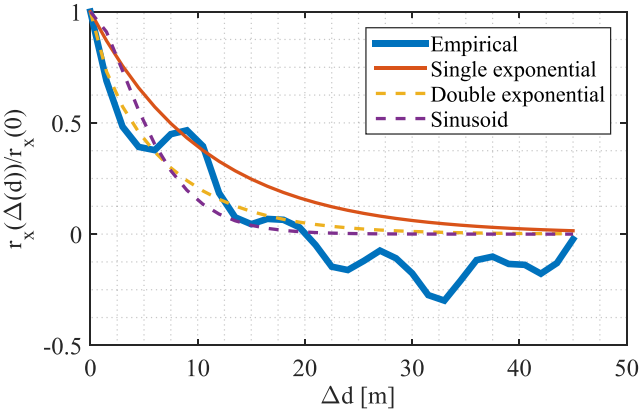

(b) OLoS part (six vehicles are obstructing the LoS).

FIGURE 16. Normalized empirical spatial autocorrelation function of shadow fading for the LoS and OLoS parts of the NLoS scenario, and the corresponding fitting models.

TABLE 3. Spatial correlation models' parameters.

Model	Par	LoS	NLoS	OLoS part	LoS part
Single exponential	d_{c1}	7.2 m	10.4 m	10.7 m	10.9 m
	σ	0.12	0.13	0.083	0.13
Double exponential	d_{c2}	5 m	7 m	1 m	8 m
	d_{c3}	5 m	7 m	7 m	8 m
	α	0.1	0.1	0.13	0.1
	σ	0.11	0.11	0.080	0.11
Sinusoid	d_{c4}	16 m	30 m	3 m	23 m
	d_{c5}	6 m	8 m	46 m	9 m
	σ	0.04	0.03	0.084	0.03

spatially correlated shadow fading, the uncorrelated shadow fading is generated with a resolution equal to the decorrelation distance. The spatial correlation is then introduced by a spline interpolation. Alternatively, to generate more accurate shadow fading map, the provided autocorrelation models can be used to introduce the correlation.

V. CONCLUSION

In this paper, V2P channel measurements have been presented and a detailed analysis on the large-scale fading in LoS and NLoS scenarios for V2P channel has been introduced. It has been found that the two-ray pathloss model fits well the measured pathloss in the LoS scenario. In the NLoS scenario, a log-distance pathloss model has been proposed. Due to the obstruction of the LoS, the pathloss exponent is equal to 1 implying that the pathloss not only depends on the propagation distance but also on the size of the obstruction. To study the propagation loss due to the obstruction of the LoS, a 3D tool has been developed. The tool detects the diffraction edges and calculates the Fresnel-Kirchoff parameter that is used to calculate the knife-edge diffraction loss. The results show a good match between the model and the measured pathloss with a standard deviation of 4 dB. Finally, the spatial autocorrelation of shadow fading is investigated. In order to study the spatial autocorrelation, shadow fading need to be assumed stationary. Therefore, the modified reverse arrangement test is applied to test the stationarity. According to the test, the stationarity hypothesis is verified with 5% significance. Three different models have been proposed for the spatial autocorrelation function. The results show that the exponential decaying sinusoid model provides a good match to the empirical spatial autocorrelation function in both scenarios.

REFERENCES

[1] *Global Status Report on Road Safety*, World Health Organization, Geneva, Switzerland, 2018.

[2] I. Rashdan, M. Schmidhammer, F. de P. Mueller, and S. Sand, "Performance evaluation of vehicle-to-vehicle communication for cooperative collision avoidance at urban intersections," in *Proc. IEEE 86th Veh. Technol. Conf. (VTC-Fall)*, Sep. 2017, pp. 1–5.

[3] H. Q. Le, I. Rashdan, and S. Sand, "Communication protocol for platoon of electric vehicles in mixed traffic scenarios," in *Proc. IEEE 27th Annu. Int. Symp. Pers. Indoor Mobile Radio Commun. (PIMRC)*, Sep. 2016, pp. 1–5.

[4] F. de P. Müller, "Survey on ranging sensors and cooperative techniques for relative positioning of vehicles," *Sensors*, vol. 17, no. 2, p. 271, 2017.

[5] D. Geronimo, A. M. Lopez, A. D. Sappa, and T. Graf, "Survey of pedestrian detection for advanced driver assistance systems," *IEEE Trans. Pattern Anal. Mach. Intell.*, vol. 32, no. 7, pp. 1239–1258, Jul. 2010.

[6] P. Hurney, P. Waldron, F. Morgan, E. Jones, and M. Glavin, "Review of pedestrian detection techniques in automotive far-infrared video," *IET Intell. Transp. Syst.*, vol. 9, no. 8, pp. 824–832, 2015.

[7] I. Rashdan, F. de P. Müller, W. Wang, M. Schmidhammer, and S. Sand, "Vehicle-to-pedestrian channel characterization: Wideband measurement campaign and first results," in *Proc. 12th Eur. Conf. Antennas Propag. (EuCAP)*, London, U.K., Apr. 2018, pp. 1–5.

[8] G. Makhoul, R. D'Errico, and C. Oestges, "Wideband vehicle to pedestrian propagation channel characterization and modeling," in *Proc. 12th Eur. Conf. Antennas Propag. (EuCAP)*, London, U.K., Apr. 2018, pp. 1–4.

[9] M. G. Doone and S. L. Cotton, "First-order characteristics of the person-to-vehicle channel at 5.8 GHz," in *Proc. 8th Eur. Conf. Antennas Propag. (EuCAP)*, Apr. 2014, pp. 848–851.

[10] J. J. Anaya, P. Merdrignac, O. Shagdar, F. Nashashibi, and J. E. Naranjo, "Vehicle to pedestrian communications for protection of vulnerable road users," in *Proc. IEEE Intell. Vehicle Symp.*, Jun. 2014, pp. 1037–1042.

[11] Z. Liu, Z. Liu, Z. Meng, X. Yang, L. Pu, and L. Zhang, "Implementation and performance measurement of a V2X communication system for vehicle and pedestrian safety," *Int. J. Distrib. Sensor Netw.*, vol. 12, no. 9, 2016, Art. no. 9.

[12] X. Wu, R. Miucic, S. Yang, S. Al-Stouhi, J. Misener, S. Bai, and W.-H. Chan, "Cars talk to phones: A DSRC based vehicle-pedestrian safety system," in *Proc. IEEE 80th Veh. Technol. Conf. (VTC-Fall)*, Sep. 2014, pp. 1–7.

[13] M. Jutila, J. Scholliers, M. Valta, and K. Kujanpää, "ITS-G5 performance improvement and evaluation for vulnerable road user safety services," *IET Intell. Transp. Syst.*, vol. 11, no. 3, pp. 126–133, 2017.

[14] P. Sewalkar, S. Krug, and J. Seitz, "Towards 802.11 p-based vehicle-to-pedestrian communication for crash prevention systems," in *Proc. 9th Int. Congr. Ultra Mod. Telecommun. Control Syst. Workshops (ICUMT)*, Nov. 2017, pp. 404–409.

[15] K. David and A. Flach, "Car-2-X and pedestrian safety," *IEEE Veh. Technol. Mag.*, vol. 5, no. 1, pp. 70–76, Mar. 2010.

[16] M. Bagheri, M. Siekkinen, and J. K. Nurminen, "Cloud-based pedestrian road-safety with situation-adaptive energy-efficient communication," *IEEE Intell. Transp. Syst. Mag.*, vol. 8, no. 3, pp. 45–62, Jul. 2016.

[17] M. Bagheri, M. Siekkinen, and J. K. Nurminen, "Cellular-based vehicle to pedestrian (V2P) adaptive communication for collision avoidance," in *Proc. Int. Conf. Connected Vehicles Expo (ICCVE)*, Nov. 2014, pp. 450–456.

[18] G. L. Turin, F. D. Clapp, T. L. Johnston, S. B. Fine, and D. Lavry, "A statistical model of urban multipath propagation," *IEEE Trans. Veh. Technol.*, vol. VT-21, no. 1, pp. 1–9, Feb. 1972.

[19] T. S. Rappaport, *Wireless Communications: Principles and Practice*, vol. 2. Upper Saddle River, NJ, USA: Prentice-Hall, 1996.

[20] R. He, B. Ai, Z. Zhong, A. F. Molisch, R. Chen, and Y. Yang, "A measurement-based stochastic model for high-speed railway channels," *IEEE Trans. Intell. Transp. Syst.*, vol. 16, no. 3, pp. 1120–1135, Jun. 2015.

[21] J. Karedal, N. Czink, A. Paier, F. Tufvesson, and A. F. Molisch, "Path loss modeling for vehicle-to-vehicle communications," *IEEE Trans. Veh. Technol.*, vol. 60, no. 1, pp. 323–328, Jan. 2011.

[22] M. Boban, W. Viriyasitavat, and O. Tonguz, "Modeling vehicle-to-vehicle line of sight channels and its impact on application-level performance metrics," in *Proc. Int. Workshop Veh. Inter-Netw. (VANET) Poster*, 2013, pp. 91–94.

[23] S. Salous, *Radio Propagation Measurement and Channel Modelling*. Hoboken, NJ, USA: Wiley, 2013.

[24] K. D. Mielenz, "Computation of Fresnel integrals. II," *J. Res. Nat. Inst. Standards Technol.*, vol. 105, no. 4, p. 589–590, 2000.

[25] J. Epstein and D. W. Peterson, "An experimental study of wave propagation at 850 Mc," *Proc. IRE*, vol. 41, no. 5, pp. 595–611, May 1953.

[26] M. Luo, G. Villemaud, and J.-M. Gorce, "Generation of 2D correlated random shadowing based on the deterministic MR-FDPF model," *EURASIP J. Wireless Commun. Netw.*, vol. 2015, no. 1, p. 208, 2015.

[27] I. Forkel, M. Schinnenburg, and M. Ang, "Generation of two-dimensional correlated shadowing for mobile radio network simulation," *WPMC*, vol. 21, p. 43, Sep. 2004.

[28] T. Abbas and K. Sjöberg, J. Karedal, and F. Tufvesson, "A measurement based shadow fading model for vehicle-to-vehicle network simulations," *Int. J. Antennas Propag.*, vol. 2015, May 2015, Art. no. 190607.

[29] T. W. Beck, T. J. Housh, J. P. Weir, J. T. Cramer, V. Vardaxis, G. O. Johnson, J. W. Coburn, M. H. Malek, and M. Mielke, "An examination of the runs test, reverse arrangements test, and modified reverse arrangements test for assessing surface EMG signal stationarity," *J. Neurosci. Methods*, vol. 156, nos. 1–2, pp. 242–248, 2006.

[30] M. Gudmundson, "Correlation model for shadow fading in mobile radio systems," *Electron. Lett.*, vol. 27, no. 23, pp. 2145–2146, Nov. 1991.

[31] T. B. Sorensen, "Correlation model for slow fading in a small urban macro cell," in *Proc. 9th IEEE Int. Symp. Pers. Indoor Mobile Radio Commun.*, vol. 3, Sep. 1998, pp. 1161–1165.

[32] Y. Zhang, J. Zhang, D. Dong, X. Nie, G. Liu, and P. Zhang, "A novel spatial autocorrelation model of shadow fading in urban macro environments," in *Proc. IEEE Global Telecommun. Conf.*, Nov./Dec. 2008, pp. 1–5.

IBRAHIM RASHDAN (M'16) received the B.Sc. degree in electronics and communication engineering from Damascus University, Damascus, Syria, in 2009, and the M.Sc. degree in electrical communication engineering from Kassel University, Kassel, Germany, in 2014. He is currently pursuing the Ph.D. degree in communication engineering with the Technical University of Berlin, Berlin, Germany. Since 2015, he has been a member of the Scientific Staff of the Institute of Communications and Navigation, German Aerospace Center. His research interests include vehicular communication, vulnerable road user safety, and channel modeling.

FABIAN DE PONTE MÜLLER (M'15) received the engineering degree in telecommunications from the University of Málaga, Spain, in 2008, and the Ph.D. degree from the School of Informatics and Mathematics, University of Passau, Germany, in 2017. He is currently a Senior Researcher with the Vehicular Application Group, German Aerospace Center (DLR),Institute of Communications and Navigation, Oberpfaffenhofen, Germany, being responsible for the activities regarding V2X Communication and vehicular localization. In the context of ITS and safety critical applications, his topics of interest include next-generation enhancements for V2X communication, vulnerable road user safety, vehicular and pedestrian localization, GNSS positioning, and Bayesian sensor fusion algorithms.

THOMAS JOST (M'11) received the Diploma degree in electrical engineering from the University of Applied Science Wiesbaden, Germany, in 2001, and the Diploma degree in electrical engineering and information technology from the Technical University of Darmstadt, Germany, in 2003, and the Ph.D. degree from the University of Vigo, Spain, in 2013. From 2003 to 2006, he held a research assistant position with the Signal Processing Group, TU Darmstadt. From 2006 to 2018, he was a member of the Scientific Staff of the Institute of Communications and Navigation, German Aerospace Center. Since 2019, he is currently with Continental AG on radar systems.

STEPHAN SAND (SM'10) received the M.Sc. degree in electrical engineering from the University of Massachusetts Dartmouth, Dartmouth, MA, USA, in 2001, the Dipl.Ing. degree in communications technology from the University of Ulm, Germany, in 2002, and the Ph.D. degree from ETH Zurich, Switzerland, in 2010. Since 2002, he has been working in several national and international research projects on wireless communications and multisensor navigation at the Institute of Communications and Navigation, German Aerospace Center, Oberpfaffenhofen, Germany. Since 2014, he has been leading the Vehicular Applications Group and researching novel systems that combine robust navigation and wireless communications technologies for road users and railways. These systems will protect vulnerable road users and increase traffic efficiency and safety in railways. He has authored or coauthored more than 100 technical and scientific publications in conferences and journals, including two books. He holds several patents on his inventions. He actively contributes to vehicular and railway communication standardization, e.g., in ETSI TC ITS and the IEEE 802.11bd Task Group.

GIUSEPPE CAIRE (S'92–M'94–SM'03–F'05) was born in Torino, in 1965. He received the B.Sc. degree in electrical engineering and the Ph.D. degree from the Politecnico di Torino, in 1990 and 1994, respectively, and the M.Sc. degree in electrical engineering from Princeton University, in 1992.

He has been a Postdoctoral Research Fellow with the European Space Agency (ESTEC), Noordwijk, The Netherlands, from 1994 to 1995, an Assistant Professor in telecommunications with the Politecnico di Torino, an Associate Professor with the University of Parma, Italy, a Professor with the Department of Mobile Communications with the Eurecom Institute, Sophia Antipolis, France, a Professor of Electrical Engineering with the Viterbi School of Engineering, University of Southern California, Los Angeles. He is currently an Alexander von Humboldt Professor with the Faculty of Electrical Engineering and Computer Science, Technical University of Berlin, Germany. He received the Jack Neubauer Best System Paper Award from the IEEE Vehicular Technology Society, in 2003, the IEEE Communications Society & Information Theory Society Joint Paper Award, in 2004 and 2011, the Leonard G. Abraham Prize for Best IEEE JSAC Paper, in 2019, the Okawa Research Award, in 2006, the Alexander von Humboldt Professorship, in 2014, the Vodafone Innovation Prize, in 2015, and an ERC Advanced Grant, in 2018. He has served for the Board of Governors of the IEEE Information Theory Society, from 2004 to 2007, and as an Officer, from 2008 to 2013. He was the President of the IEEE Information Theory Society, in 2011. His research interests include communications theory, information theory, and channel and source coding with particular focus on wireless communications.